Article

Multi-Functional Potassium Ion Assists Ammonium Vanadium Oxide Cathode for High-Performance Aqueous Zinc-Ion Batteries

Dan He [ID], Tianjiang Sun, Qiaoran Wang, Tao Ma, Shibing Zheng, Zhanliang Tao * and Jing Liang *

Key Laboratory of Advanced Energy Materials Chemistry (Ministry of Education), Haihe Laboratory of Sustainable Chemical Transformations, Renewable Energy Conversion and Storage Center, College of Chemistry, Nankai University, Tianjin 300071, China
* Correspondence: taozhl@nankai.edu.cn (Z.T.); liangjing@nankai.edu.cn (J.L.); Tel.: +86-22-23504486 (Z.T. & J.L.)

Abstract: Ammonium vanadium oxide ($NH_4V_4O_{10}$) is a promising layered cathode for aqueous zinc-ion batteries owing to its high specific capacity (>300 mA h g^{-1}). However, the structural instability causes serious cycling degradation through irreversible insertion/extraction of NH_4^+. Herein, a new potassium ammonium vanadate $K_x(NH_4)_{1-x}V_4O_{10}$ (named KNVO) is successfully synthesized by a one-step hydrothermal method. The inserted of K^+ can act as structural pillars, connect the adjacent layers closer and partially reduce the de-insertion of NH_4^+. Due to the multi-functional of K^+, the prepared KNVO presents a high specific discharge capacity of 432 mA h g^{-1} at a current density of 0.4 A g^{-1}, long cycle stability (2000 cycles, 94.2%) as well as impressive rate performance (200 mA h g^{-1} at 8 A g^{-1}).

Keywords: aqueous zinc-ion batteries; cathode materials; vanadium-based; potassium ammonium vanadate

1. Introduction

In recent years, aqueous zinc ion batteries (AZIBs) are considered as promising candidates for grid-scale energy storage because of their low cost, high operational safety, and environmentally friendly [1–3]. Cathode materials are related to the operating voltage, cycling stability, and rate performance in AZIBs. Therefore, developed high-performance cathode materials have become a breakthrough point in the large-scale application of AZIBs. Previously, various cathode materials have been developed in AZIBs including vanadium-based materials [4–6], manganese-based compounds [7–9], Prussian blue analogues [10,11], and organic compounds [12–15], and others. Among these reported cathode materials, vanadium-based materials with high capacity (>300 mA h g^{-1}), various oxidation states (V^{5+}, V^{4+}, and V^{3+}), and several coordination polyhedra (VO_4, VO_5, and VO_6), are widely studied in AZIBs [16]. Among these reported vanadium-based materials. For instance, layer-type V_2O_5 [17] and its derivative $NH_4V_4O_{10}$, [18] tunnel-type VO_2 [19], 3D open framework-type $Na_3V_2(PO_4)_3$ [20], etc. It is worth noting that the layered type $NH_4V_4O_{10}$ (NVO) has a high specific capacity due to the high oxidation of V. NH_4^+ has a large ion radius and small mass, corresponding to large bi-layered NVO interlayer spacing for facile ion intercalation and storage. Therefore, it has faster ionic transfer dynamics and higher energy density to some extent in comparison with V_2O_5. But some areas still need to be improved for it. Firstly, the electrostatic interaction of NH_4^+ and V-O layer is weak while the force between Zn^{2+} and the host materials is strong. The inserted Zn^{2+} inevitably extrudes NH_4^+ [21], leading to structural deformations and forming large migration barriers for the diffusion of Zn^{2+}, further resulting in poor cycling stability [22–24] and limited rate performance. In addition, the electrochemical performance of NVO is affected by the inherently low electrical conductivity [25]. Heretofore, many strategies have been reported to solve these problems. For instance, inserting cations or water molecules between layers [26–29], composing nanomaterials [30], coating conductive materials [21], and others.

Among the above strategies, it has been confirmed that the cations (such as single cations [31] or dual ions) accesses interlayer is an effective strategy. For example, $K_{1.1}V_3O_8$ was reported as high-performance AZIBs cathode, which exhibits high specific capacity (386 mA h g^{-1}), long cycle performance (>1000 cycles), and excellent rate performance [32]. Feng et al. reported that the insertion of K$^+$ greatly improves the electrochemical performance of $MgV_2O_5 \cdot nH_2O$ [33]. Such impressive performance was mainly attributed to the following: (1) K$^+$ has a low diffusion energy barrier and high lattice energy barrier, it could support and stabilize the crystal structure. (2) Metal ions bonded with oxygen atoms bring about strong ionic bonds, thus K$^+$ can make the connection between V-O layers closer and stabilize the structure of the material. (3) The insertion of K$^+$ can improve the electrical conductivity of the material. To take advantage of these features, herein, we report on a synthesis of K$^+$ pre-inserted $NH_4V_4O_{10}$ bi-layered type $K_x(NH_4)_{1-x}V_4O_{10}$ material (named KNVO) via a facile one-step hydrothermal method, and show its outstanding electrochemical performance as a new cathode for AZIBs. K$^+$ was selected to be pre-inserted into the NVO layer because of their smaller radius of K$^+$ (1.33 Å) in comparison with NH$_4^+$ (1.43 Å), and K$^+$ bonded with oxygen brings about strong ionic bonds, thus K$^+$ can make the connection between V-O layers closer and stabilize the structure of the material. NH$_4^+$ has a multistage tetrahedron structure, when K$^+$ is embedded, the force between K$^+$ and structure O made the layer spacing reduced. The positive ions interaction between K$^+$ and NH$_4^+$ causes the direction of hydrogen in NH$_4^+$ to change, and the reduced layer spacing causes the distance between H and structure O shortened, which not only could promote hydrogen bond formation of N-H . . . O, but also maintain this interaction force. So the inserted K$^+$ partially prevents ammonium de-insertion from KNVO. The hydrogen bond interaction between host O and NH$_4^+$ facilitates the diffusion kinetics and maintains the integrity of the structure. Benefited by them, the prepared KNVO presents a higher specific capacity of 432 mA h g^{-1} (0.4 A g^{-1}), longer cycle stability (2000 cycles, 94.2%) as well as more impressive rate performance.

2. Experimental

2.1. The Synthesis of KNVO

The KNVO was synthesized via a simple hydrothermal method. In a typical procedure, 10.0 mmol oxalic acid and 5.0 mmol ammonium metavanadate was dissolved in 30 mL deionized water, and then 2.5 mmol potassium nitrate was added into the solution under stirring at room temperature for 2 h. After that, the mixture solution was transferred into a 50 mL Teflon-lined stainless autoclave, sealed, and kept at 180 °C for 18 h. The product was filtered, washed with a great deal of deionized water and ethyl alcohol, and lastly dried at 60 °C for 12 h.

2.2. The Synthesis of NVO

In a simple hydrothermal method, 2.74 mmol ammonium metavanadate was dissolved in 40 mL deionized water under stirring at room temperature for 10 min, and then 2.50 mmol oxalic acid was added into the solution under stirring at room temperature for 0.5 h. Lastly, the mixture solution was transferred into a 50 mL Teflon-lined stainless autoclave, sealed, and kept at 180 °C for 3 h. The product was filtered, washed with a great deal of deionized water and ethyl alcohol, and lastly dried at 60 °C for 12 h.

3. Results and Discussion

The crystalline phases of the NVO (JCPDF No. 31-0075) and KNVO samples are examined by using X-ray diffraction (XRD) and the results are shown in Figure 1a. The XRD patterns of NVO and KNVO are indexed to a monoclinic NVO phase with a space group of C2/m and no characteristic peaks of impurities are detected. Besides, the strong peak at 8.7° of NVO corresponds to the (001) plane with an interlayer spacing of 10.1 Å. When K$^+$ is added into NVO, the (001) peak slightly shifts toward a higher degree (9.3°), indicating the shrinkage of interplanar spacing. According to the reported literature, it

could be attributed to the stronger electrostatic interaction between K^+ and O^{2-} [34] and the small ion radius of K ions (133 pm of K^+ and 143 pm of NH_4^+). Figure 1b appears the Crystal structural illustration of KNVO, the monoclinic phase of it with a space group of C2/m and there are two ions (K^+ and NH_4^+) embedded between the layers. The Fourier transform infrared (FT-IR) spectrum of KNVO is shown in Figure 1c. The peak at 971 cm^{-1} is a typical stretching of V=O bonds. The peak at 758 cm^{-1} is the vibrations of V-O-V chains, and the peak at about 501 cm^{-1} belongs to the bending vibrations of V-O [35–37]. Besides, the peaks situated at 1409 and 3161 cm^{-1} are ascribed to the bending and stretching vibration of N-H bonds, respectively [35]. The (FT-IR) spectrum of NVO is presented in Figure S1, all the other peaks correspond well except for the N-H bond. Compared with NVO, the N-H bond of KNVO is offset to a high wave number, which means that the insertion of K^+ has some effect at NH_4^+. Figure S2 presents the Raman spectra of KNVO, the peak at 261 cm^{-1} belongs to the K-O bond [34], proving the K-O ion bond exists. The X-ray photoelectron spectroscopy (XPS) in Figure 1d. The V $2p_{3/2}$ in the NVO has two peaks at 515.75 eV and 517.45 eV, corresponding to V^{4+} and V^{5+} [38,39]. The V $2p_{3/2}$ in the KNVO also has two peaks at 515.75 eV and 517.48 eV. The peaks of V^{4+} and V^{5+} in NVO and KNVO are not shift, which indicated the insertion of K^+ only replaced part of NH_4^+ and not changed the valence of V. In addition, the V^{4+} and V^{5+} in NVO and KNVO coexist with an approximate ratio of 1:3, proving the average valence state of 4.75, which can provide a high theoretical specific capacity. The morphology and microstructure of KNVO are characterized by scanning electron microscope (SEM) and transmission electron microscopy (TEM). The SEM image (Figure 1e,f) shows that the prepared sample is rounded clusters by stacking petal sheets structure with a particle size of ~1 μm. As shown in Figure 1g, the TEM image of $KNH_4V_4O_{10}$ shows the details of the rounded clusters, which are composed of stacked sheets. In Figure 1h and Figure S3 the high-resolution TEM (HRTEM) image shows clear lattice fringes and the regular spacing is 0.95 nm, corresponding well to the d $_{(001)}$ spacing from the XRD pattern in Figure 1a. As is shown in Figure 1i, the energy-dispersive spectroscopy (EDS) elemental mapping images show that the K, N, V, and O elements are uniformly distributed in KNVO nanoparticles, and the K 2p XPS spectrum of KNVO exhibits two peaks (Figure S4), which can be ascribed to K $2p_{1/2}$ (295.2 eV) and K $2p_{3/2}$ (292.4 eV) [40], manifesting the successful insertion of K^+ into NVO. Figure S5 shows the high-resolution O 1s spectrum of KNVO in pristine, discharged to 0.2 V, and charged to 1.6 V, respectively. It indicates that the peaks at 529.5, and 530.4 eV, correspond to V-O and O-H bonds [41], respectively. It is of great benefit to the improvement of KNVO electrochemical performance.

In order to evaluate the electrochemical performance of the material after doping into K^+, the aqueous zinc-ions battery consisting of Zn-metal anode, 3 mol L^{-1} $Zn(CF_3SO_3)_2$ electrolyte, and glass fiber separator is fabricated and shown in Figure 2a. Figure 2b shows the first five cyclic voltammetry (CV) curves of the Zn//KNVO battery at a scan rate of 0.5 m V s^{-1} and the voltage is between 0.2 and 1.6 V (vs. Zn^{2+}/Zn). There are two obvious pairs of reduction/oxidation peaks at 0.49/0.75 and 0.91/1.11 V (vs. Zn^{2+}/Zn), proving the multiple insertion/extraction processes of ion storage in KNVO. In addition, the small redox peaks at 1.35 V could be possibly assigned to the NH_4^+ (de)-intercalation [29]. And these redox peaks correspond well to the voltages of the charging/discharging platform, as shown in Figure 2d, and at a current density of 0.4 A g^{-1}, from the 1st to the 50th, the specific discharge capacity gradually increases from 313 mA h g^{-1} to 400 mA h g^{-1}. It is discovered that the first CV curve displays some variations compared to the latter. Moreover, apart from the first discharge curve, the rest discharge and charge curves are overlapping, indicating the nature of the high reversibility of Zn^{2+} storage. For the Zn//KNVO battery, Figure 2c shows the rate performance of the KNVO and NVO electrodes, respectively. The NVO battery presents a poor rate performance, which mainly results from irreversible de-insertion of NH_4^+. By contrast, the discharge-specific capacities of KNVO are 432, 400, 346, 300, and 215 mA h g^{-1} at current densities of 0.2, 0.5, 1, 2, and 5 A g^{-1}, respectively, rooted in more impressive rate performance. Even at a high current density of 8 A g^{-1}, it also

exhibits an excellent discharge capacity of 200 mA h g^{-1}. This suggests that the insertion of K$^+$ made KNVO a faster Zn^{2+} storage ability. In addition, the specific capacity can go back to 430 mA h g^{-1} when the current density returns to 0.2 A g^{-1}, further indicating good reversibility. In addition, the KNVO electrode shows good cycling stability at a low current of 0.4 A g^{-1}. As displayed in Figure 2e, the KNVO electrode shows a high reversible capacity of 405 mA h g^{-1} after the activation process, and a high capacity retention ratio of 92.1% is obtained after 100 cycles. However, from the 1st to the 15th, the specific discharge capacity decreases fast for the Zn//NVO battery. It is even more regrettable that its capacity retention only has 50% after 50 cycles, which indicates the KNVO material possesses a more stable crystal structure due to the introduction of K$^+$ cations. Furthermore, the KNVO electrode exhibits good long cycling performance, as shown in Figure 2f. After the initial 90 cycles, the capacity of KNVO increases to a maximum capacity of 350 mA h g^{-1} at a high current density of 5 A g^{-1} due to the activation process. After 2000 cycles, a high specific capacity of 306 mA h g^{-1} can be maintained, the capacity retention is calculated to be 94.2%. For comparison, the NVO electrode exhibits lower specific capacity and poor long cyclic performance. In summary, the electrochemical performance of NVO was improved remarkably by the insertion of K$^+$. Owing to its high capacity, high-rate performance, and long cycling performance, the KNVO electrode is a promising cathode in AZIBs. Table S1 compares the voltage, specific capacity, and capacity retention of KNVO with the other reported cathodes. KNVO delivers high capacity, high-rate performance, and long cycling performance.
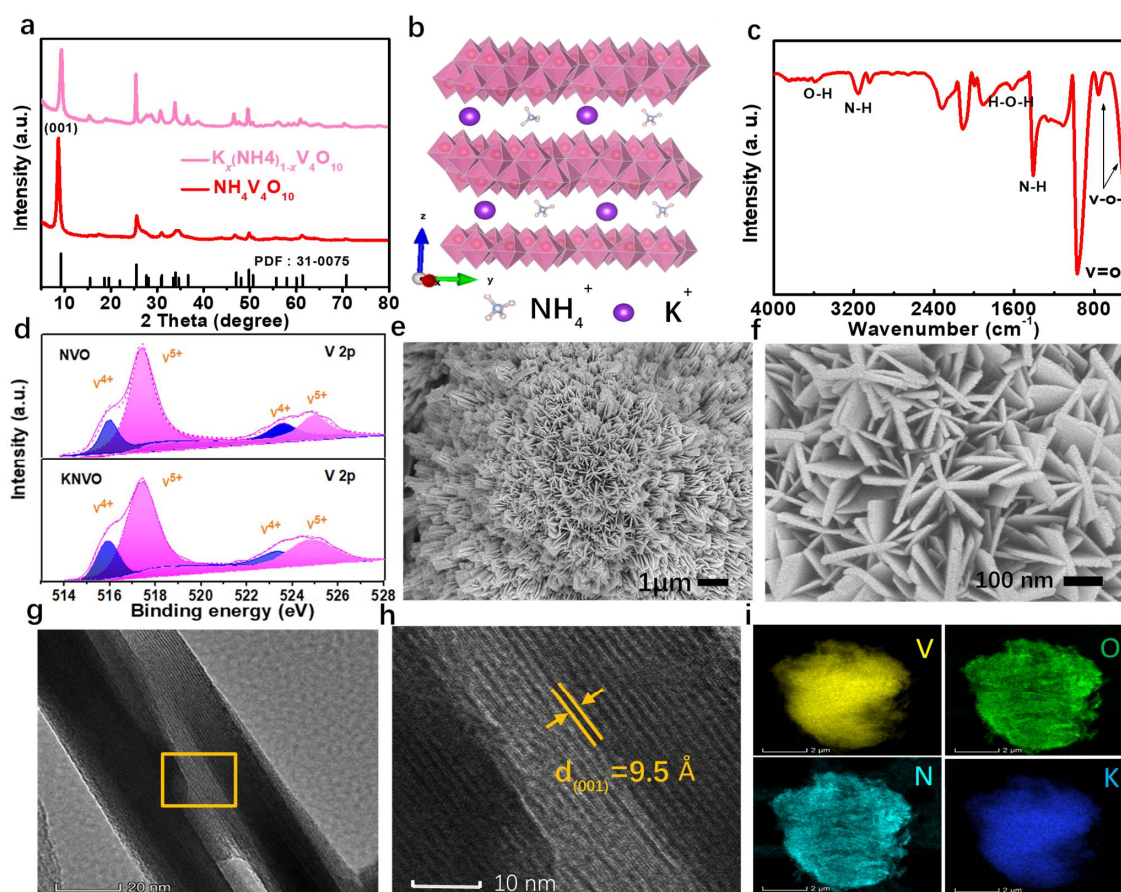

Figure 1. (**a**) XRD pattern of NVO and KNVO (**b**) Crystal structural illustration of KNH$_4$V$_4$O$_{10}$. (**c**) FTIR spectra of KNVO. (**d**) V2p XPS spectrum of NVO and KNVO. (**e**,**f**) SEM images of KNVO. (**g**–**i**) TEM, HRTEM images, and elemental mapping image of KNVO, respectively.
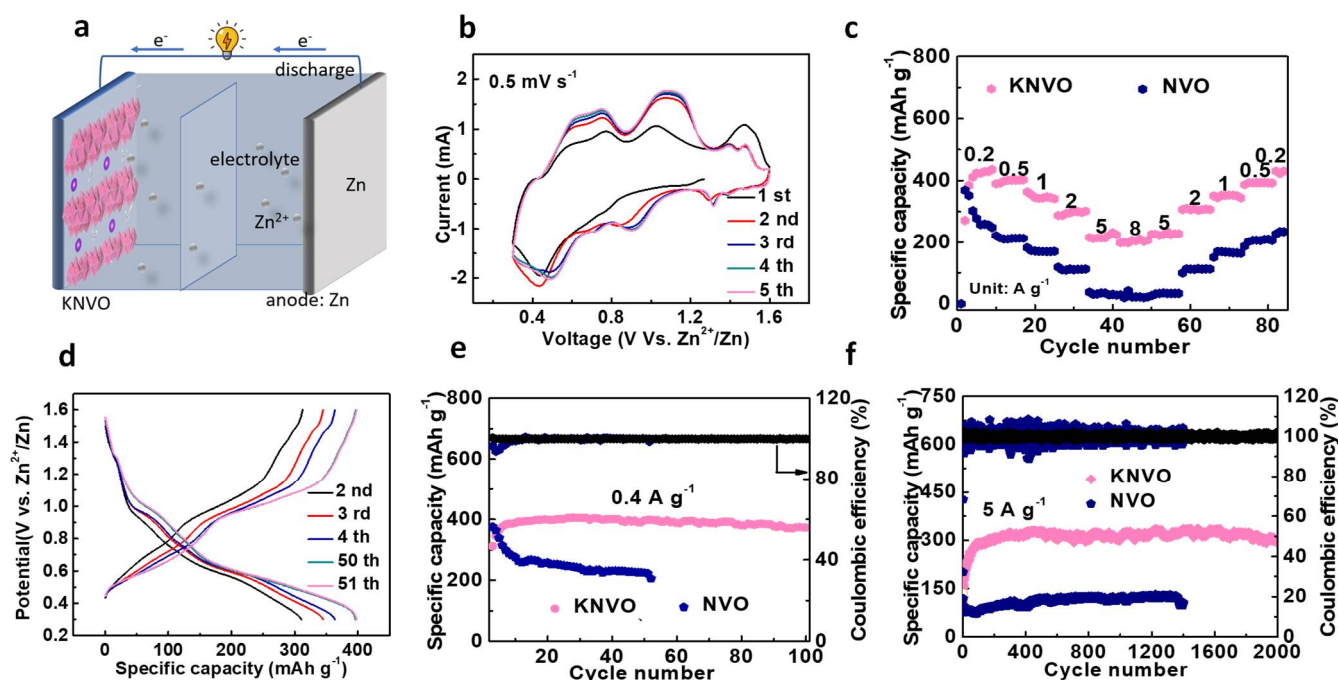
Figure 2. (**a**) Diagrammatic of the aqueous Zn//KNVO battery. (**b**) The first five cyclic voltammetry (CV) curves of KNVO at 0.5 mV s^{-1}. (**c**) Rate performance at various currents ranging from 0.5 to 8 A g^{-1}. (**d**) Charge/discharge profiles at 0.4 A g^{-1}; (**e**) Cyclic performance at 0.4 A g^{-1}. (**f**) Cyclic performance at 5 A g^{-1}.

To further understand the electrochemical kinetics of the KNVO cathode, CV tests at different scan rates from 0.2 to 0.8 mV s^{-1} are carried out (Figure 3a). As an increase in the scan rate, the relationship between the current *i* (mA) and the scan rate *ν* (mV s^{-1}) is shown in the following equation [42]:

$$i = a\nu^b \tag{1}$$

In the above equation, *a* and *b* are variable parameters and *i* is the peak current at the scan rate of *ν*. Thus, the *b* value can be obtained by calculating the slope of log(*i*) and log(*ν*), which could evaluate the electrochemical behavior of the battery. Once the *b*-value is close to 0.5, it indicates a semi-infinite linear diffusion process derived from a battery-type interaction. If the b-value is close to 1.0, it illustrates that the capacity is contributed by the capacitive-type behavior. In Figure 3b, the fitting results show that the slopes of four redox peaks are 0.65, 0.88, 0.81, and 0.71, respectively, indicating that it is a capacitive-limited process. It implies that KNVO displays mainly capacitor-like kinetics, which can be ascribed to the surface pseudocapacitance, resulting in remarkable rate performance. Following the calculated *b* values, the current can be divided into capacitive-controlling ($k_1\nu$) and diffusion-controlling ($k_2\nu^{1/2}$) contributions followed by the equations [43]:

$$i = k_1\nu + k_2\nu^{1/2} \tag{2}$$

$$i/\nu^{1/2} = k_1\nu^{1/2} + k_2 \tag{3}$$

As shown in Figure 3c, the capacitance occupied about 71.9% of the total capacity of the batteries at 0.2 mV s^{-1}. The percentage of the two sections is shown in Figure 3d, with the increase of scan rates from 0.2 to 0.8 mV s^{-1}, the capacitive contribution ratio grows from 71.9% to 90.5%, revealing that the pseudocapacitive contribution is dominant, which is in favor of high-rate performances [43–45]. In addition, the galvanostatic intermittent titration

technique (GITT) is used to investigate the Zn^{2+} diffusion coefficient of the KNVO electrode. The Zn^{2+} diffusivity ($D(Zn^{2+})$) can be calculated using the following equation [42]:

$$D = \frac{4L^2}{\pi\tau}\left(\frac{\Delta E_s}{\Delta E_t}\right)^2$$

where τ is the relaxation time. ΔE_s is the steady-state voltage change after the current pulse. ΔE_t is the voltage change (V) during the relaxation process. L is ion diffusion length (cm), which is approximately equal to the thickness of the electrode. The calculated results are presented in Figure S6, and the diffusion coefficient of Zn^{2+} in the KNVO cathode ranges from 3.22×10^{-9} to 2.27×10^{-7} cm^2 s^{-1}, indicating the fast ion diffusion kinetics of KNVO.
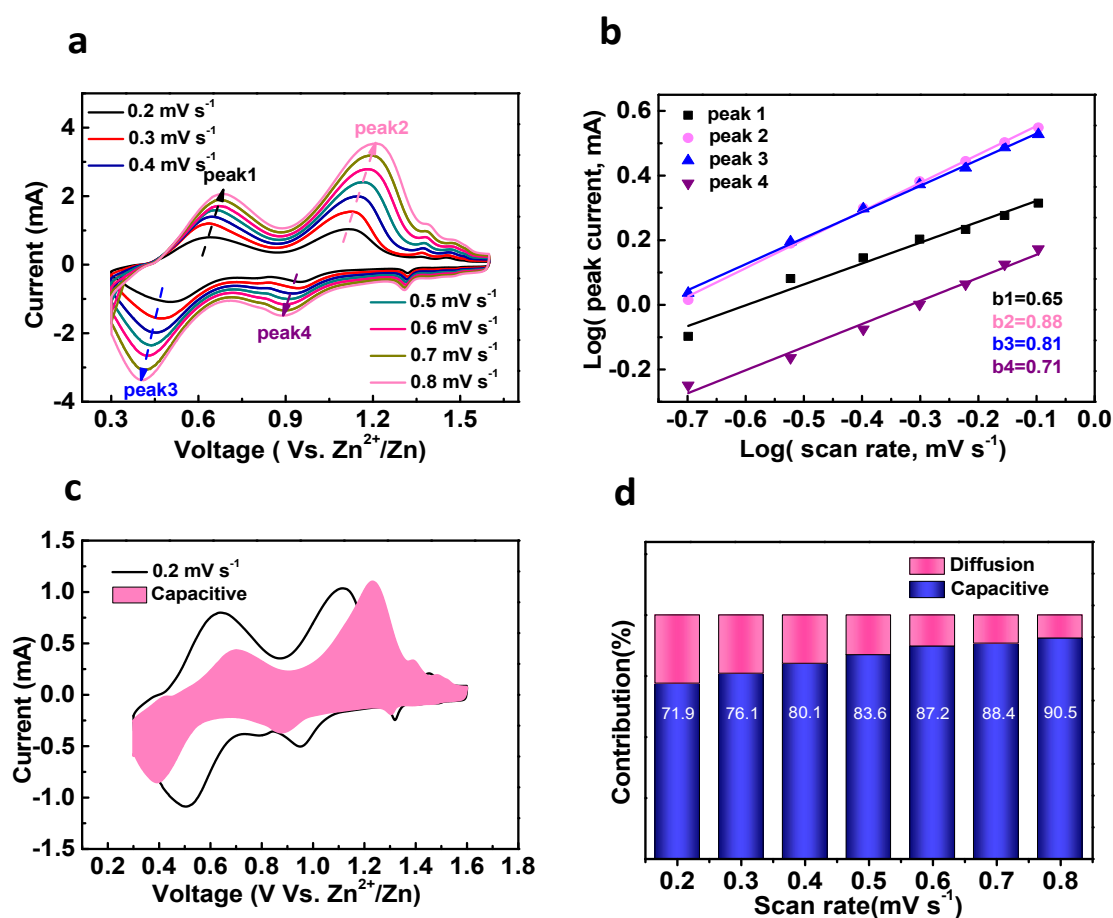

Figure 3. (**a**) CV profiles of KNVO at different scan rates from 0.2 to 0.8 mV s^{-1}. (**b**) log(i) versus log(v) curves of cathodic and anodic peaks. (**c**) Capacitive (pink line) contribution to charge storage at 0.2 mV s^{-1}. (**d**) Contribution to charge storage at different scans.

The ex situ XRD pattern is shown in Figure 4a, hereon, we further study the charge storage mechanism during charge/discharge progress. Compared with the original electrode, new diffraction peaks located at 6.7°, 18.1°, and 26.4° appear and increase when the electrode was further discharged to 0.5V and gradually increased, according to previous reports, which can be indexed to the $Zn_xOTf_y\,(OH)_{2x-y}\cdot nH_2O$ (ZTFH) [46–48], and the SEM image of it is shown in Figure S7b. The ZTFH is generated by the reaction of OH$^-$ with $Zn(CF_3SO_3)_2$ and H_2O. The OH$^-$ ions come from the dissociation of water, and the same amount of H$^+$ is generated at the same time, which is inserted into the KNVO electrode. KNVO electrode follows the co-insertion of H$^+$ and Zn^{2+} mechanism, as well as NaV_3O_8 [48]. The H$^+$ in the electrolyte is embedded in the cathode material during the discharged progress, leading to an increased pH on the surface of the cathode, so the electrolyte generates a by-product ZTFH on the surface of the cathode, and the peak of the

ZTFH gradually disappears during the charged progress, which proved a reversible phase transition process. The SEM images of KNVO in the initial (Figure S7a), fully discharged (Figure S7b), and fully charged (Figure S7c) state also indicated the reversible (de-)insertion of H^+ and Zn^{2+}. At the same time, in the enlarged XRD pattern, the diffraction peak of the (001) plane shifts slightly to lower angles at the discharged state of 0.9 V, indicating the insertion of larger radii Zn^{2+}. When fully discharged to 0.5 V, the diffraction peak of the (001) reflection shifts slightly to higher angles, indicating a smaller layer spacing. The decrease in lattice spacing is probably ascribed to an increased electrostatic interaction between bilayers and intercalation Zn^{2+}. After charging to 1.6 V, the reflection returns to its original position because of the extraction of Zn^{2+}, proving the reversible structure of the KNVO electrode during the Zn ions insertion/de-insertion progress, which is in keeping with Figure S8a,b, they showed the HRTEM of KNVO in fully discharged and charged state, respectively. In the discharged state, the lattice spacing became 0.85 nm because of the insertion of Zn^{2+}, and the interaction force between Zn^{2+} and the structure O made the layer spacing reduced. When fully charged, the layer spacing became larger at 0.94 nm due to the removal of zinc ions. Table S2 shows the element distribution of KNVO in a fully discharged and charged state, respectively. In the discharged state, due to the intercalation of Zn^{2+}, the atomic percentage of Zn^{2+} is more than the charged state. The peak at 43.6°, 50.8°, and 74.6° compounds to the stainless steel net. To further investigate the other effect of chemically inserted K^+ cations into NVO. Figures 4c and S9 show N1s ex situ XPS spectra of KNVO and NVO at a different state, respectively. For the N1s XPS spectrum of NVO (Figure S9), the peak at 401.4 eV is NH_4^+. The N 1s (Figure 4c) in the KNVO could be resolved into two peaks at 399.6 and 401.4 eV, corresponding to NH_4^+ and N-H ... O hydrogen bond [49]. Thus, by contrast, figures (Figures 4c and S10), the insertion of K^+ could promote hydrogen bond formation of N-H ... O and maintain this interaction force. This can be attributed to the that NH_4^+ has a multistage tetrahedron structure, when K^+ is embedded, the force between K^+ and structure O and due to the smaller radius of K^+ (1.33 Å) in comparison with NH_4^+ (1.43 Å) made the layer spacing reduced (shown in Figure 1a). The positive ions interaction between K^+ and NH_4^+ causes the direction of hydrogen in NH_4^+ to change, and the reduced layer spacing causes the distance between H and structure O shortened, which not only could promote hydrogen bond formation of N-H ... O, but also maintain this interaction force. So the inserted K^+ partially prevents ammonium de-insertion from KNVO. The hydrogen bond interaction between host O and NH_4^+ facilitates the diffusion kinetics and maintains the integrity of the structure. Figure 4d shows the Zn 2p XPS spectrum of KNVO in initial, fully discharged, and fully charged states, respectively. No signal of the zinc element can be detected in the pristine state. However, two strong peaks of Zn $2p_{1/2}$ (1045.3 eV) and Zn $2p_{3/2}$ (1022.1 eV) appear, respectively, confirming the successful insertion of Zn ions into the KNVO electrode. However, after being charged to 1.6 V, the intensity of Zn 2p peaks becomes far weaker, demonstrating the de-intercalation of zinc ions from the KNVO electrode. V 2p ex situ XPS spectra are shown in Figure 4e. Compared to the initial state, the intensity of the V^{5+} peak weakens and V^{4+} increases after the KNVO electrode is discharged to 0.2 V, indicating the reduction of V^{5+}. After being charged to 1.6 V, the V^{5+} signal increases, and the V^{4+} signal decreases. The EDS mapping images are shown in Figure 4f,g, after fully discharged and charged, the K, N, V, and O elements are uniformly distributed in KNVO nanoparticles. In the meantime, Table S2 shows the element distribution and atomic percentage of KNVO in a fully discharged and charged state, respectively. In the discharged state, due to the intercalation of Zn^{2+}, the atomic percentage of Zn^{2+} is more than the charged state. Besides, the proportion of K, N, V, and O elements in KNVO is stable after fully discharged and charged states, which also indicated the integrity of the structure and the reduction of irreversible NH_4^+ de-insertion after inserted K^+.
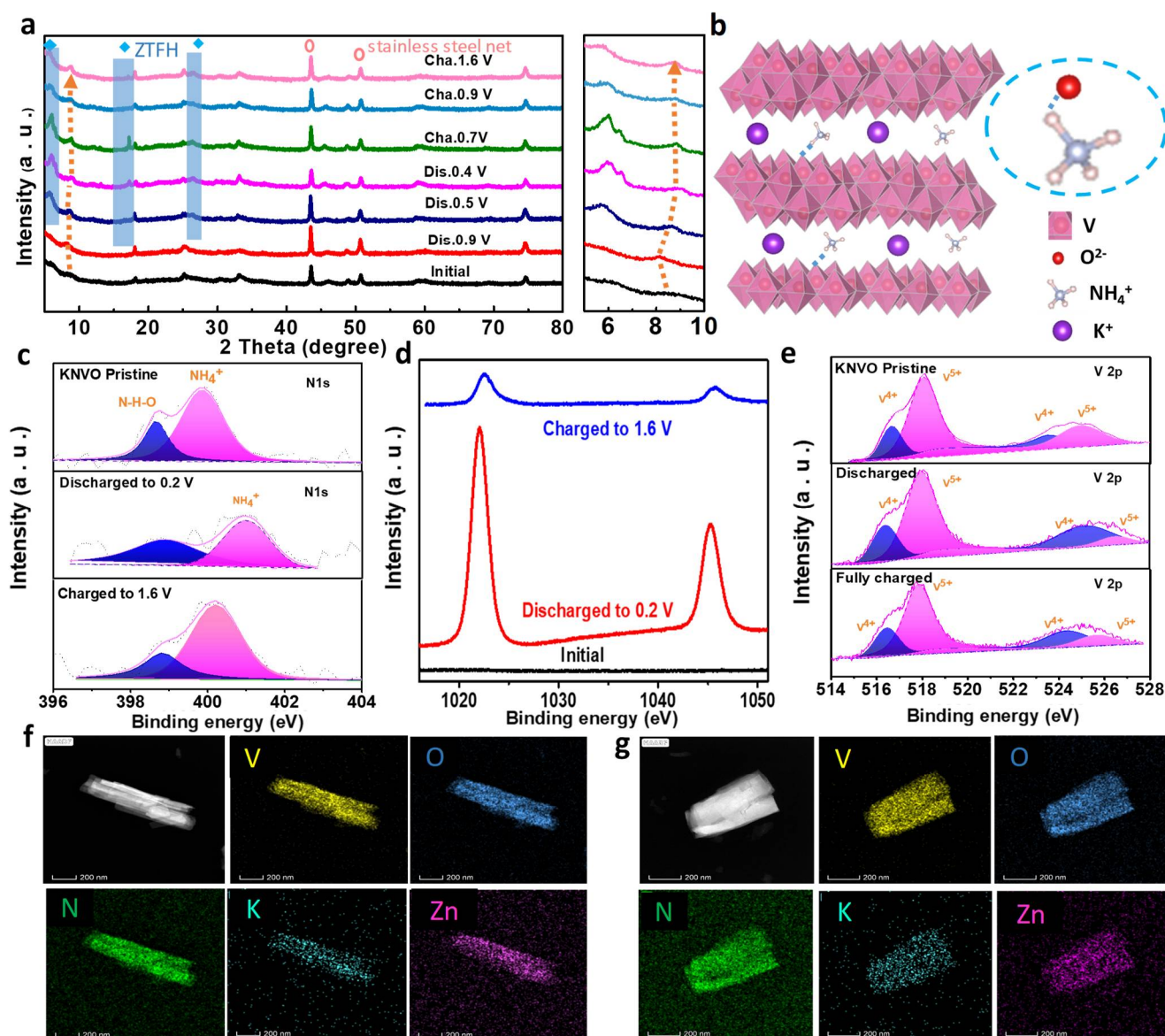
Figure 4. (**a**) The ex situ XRD (the enlarged XRD) pattern of KNVO. (**b**) Crystal structural illustration of KNVO and hydrogen bond formation in KNVO. (**c**) N1s XPS spectrum of KNVO. (**d**) Zn 2p XPS spectrum of KNVO in initial, discharged, and charged state, respectively. (**e**) V2p XPS spectrum of KNVO in initial, discharge, and charge state, respectively. (**f,g**) SEM image of KNVO in discharge, and charge state, respectively.

4. Conclusions

In summary, we designed and synthesized a KNVO cathode for AZIBs. The chemically inserted K cation into NVO could act as structural pillars. The insertion of K did not change the valence of V, thus keeping the high valence of it, which could maintain the high specific capacity of NVO to some extent. In the meantime, due to the smaller radius of K^+ in comparison with NH_4^+ and K^+ bonded with oxygen bringing about strong ionic bonds, K^+ can make the connection between V-O layers closer and stabilize the structure of the material, which promotes the hydrogen bond formation of N-H ... O and maintains this interaction force. The inserted K^+ partially prevents ammonium de-insertion from KNVO, maintaining the integrity of the structure. Benefited by them, it achieves a more impressive rate of performance and cyclability than NVO cathode materials in zinc-ion batteries. In addition, it follows the H^+, Zn^{2+} co-insertion mechanism. Our work reports a dual ions material for zinc ion batteries and provides a design idea for future high-performance cathodes.

References

1. Du, M.; Liu, C.; Zhang, F.; Dong, W.; Zhang, X.; Sang, Y.; Wang, J.J.; Guo, Y.G.; Liu, H.; Wang, S. Tunable Layered (Na, Mn)V_8O_{20}·nH_2O Cathode Material for High-Performance Aqueous Zinc Ion Batteries. *Adv. Sci.* **2020**, *7*, 2000083. [CrossRef]
2. Wang, Q.; Sun, T.; Zheng, S.; Li, L.; Ma, T.; Liang, J. A New Tunnel-type V_4O_9 Cathode for High Power Density Aqueous Zinc ion Batteries. *Inorg. Chem. Front.* **2021**, *8*, 4497–4506. [CrossRef]
3. Tang, B.; Shan, L.; Liang, S.; Zhou, J. Issues and Opportunities Facing Aqueous Zinc-Ion Batteries. *Energy Environ. Sci.* **2019**, *12*, 3288–3304. [CrossRef]
4. Zhu, K.; Wu, T.; Huang, K. A High Capacity Bilayer Cathode for Aqueous Zn-Ion Batteries. *ACS Nano* **2019**, *13*, 14447–14458. [CrossRef]
5. Liu, S.; Zhu, H.; Zhang, B.; Li, G.; Zhu, H.; Ren, Y.; Geng, H.; Yang, Y.; Liu, Q.; Li, C.C. Tuning the Kinetics of Zinc Ion Insertion/Extraction in V_2O_5 by In Situ Polyaniline Intercalation Enables Improved Aqueous Zinc-Ion Storage Performance. *Adv. Mater.* **2020**, 2001113. [CrossRef]
6. Wang, B.; Yan, J.; Zhang, Y.; Ye, M.; Yang, Y.; Li, C.C. In Situ Carbon Insertion in Laminated Molybdenum Dioxide by Interlayer Engineering Toward Ultrastable "Rocking Chair" Zinc-Ion Batteries. *Adv. Funct. Mater.* **2021**, *31*, 2102827. [CrossRef]
7. Xu, C.; Li, B.; Du, H.; Kang, F. Energetic Zinc Ion Chemistry: The Rechargeable Zinc Ion Battery. *Angew. Chem. Int. Ed.* **2012**, *51*, 933–935. [CrossRef]
8. Liu, Z.; Wang, D.; Tang, Z.; Liang, G.; Yang, Q.; Li, H.; Ma, L.; Mo, F.; Zhi, C. A Mechanically Durable and Device-Level tough Zn-MnO_2 Battery with High Flexibility. *Energy Storage Mater.* **2019**, *23*, 636–645. [CrossRef]
9. Sun, T.; Nian, Q.; Zheng, S.; Shi, J.; Tao, Z. Layered $Ca_{0.28}MnO_2$·0.5H_2O as a High Performance Cathode for Aqueous Zinc-Ion Battery. *Small* **2020**, *16*, e2000597. [CrossRef]
10. Wessells, C.D.; Huggins, R.A.; Cui, Y. Copper Hexacyanoferrate Battery Electrodes with Long Cycle Life and High Power. *Nat. Commun.* **2011**, *2*, 550. [CrossRef]
11. Ge, J.; Fan, L.; Rao, A.; Zhou, J.; Lu, B. Surface-substituted Prussian blue analogue cathode for sustainable potassium-ion batteries. *Nat. Sustain.* **2022**, *5*, 225–234. [CrossRef]
12. Chae, M.S.; Hong, S.-T. Prototype System of Rocking-Chair Zn-Ion Battery Adopting Zinc Chevrel Phase Anode and Rhombohedral Zinc Hexacyanoferrate Cathode. *Batteries* **2019**, *5*, 3–13. [CrossRef]
13. Chifotides, H.T.; Schottel, B.L.; Dunbar, K.R. The p-Accepting Arene HAT(CN)$_6$ as a Halide Receptor through Charge Transfer: Multisite Anion Interactions and Self-Assembly in Solution and the Solid State. *Angew. Chem. Int. Ed.* **2010**, *49*, 7202–7207. [CrossRef] [PubMed]
14. Zheng, S.; Wang, Q.; Hou, Y.; Li, L.; Tao, Z. Recent Progress and Strategies toward High Performance Zinc-Organic Batteries. *J. Energy Chem.* **2021**, *63*, 87–112. [CrossRef]
15. Zheng, S.; Shi, D.; Yan, D.; Wang, Q.; Sun, T.; Ma, T.; Li, L.; He, D.; Tao, Z. Orthoquinone-Based Covalent Organic Frameworks with Ordered Channel Structures for Ultrahigh Performance Aqueous Zinc-Organic Batteries. *Angew. Chem. Int. Ed.* **2022**, *61*, e202117511. [CrossRef]
16. Liao, M.; Wang, J.; Ye, L.; Sun, H.; Wen, Y.; Wang, C.; Sun, X.; Wang, B.; Peng, H. A Deep-Cycle Aqueous Zinc-Ion Battery Containing an Oxygen-Deficient Vanadium Oxide Cathode. *Angew. Chem. Int. Ed.* **2020**, *59*, 2273–2278. [CrossRef]

17. Yan, M.; He, P.; Chen, Y.; Wang, S.; Wei, Q.; Zhao, K.; Xu, X.; An, Q.; Shuang, Y.; Shao, Y.; et al. Water-Lubricated Intercalation in $V_2O_5 \cdot nH_2O$ for High-Capacity and High-Rate Aqueous Rechargeable Zinc Batteries. *Adv. Mater.* **2018**, *30*, 1703725. [CrossRef]

18. Li, Q.; Rui, X.; Chen, D.; Feng, Y.; Xiao, N.; Gan, L.; Zhang, Q.; Yu, Y.; Huang, S. A High-Capacity Ammonium Vanadate Cathode for Zinc-Ion Battery. *Nano Micro Lett.* **2020**, *12*, 67. [CrossRef]

19. Ding, J.; Du, Z.; Gu, L.; Li, B.; Wang, L.; Wang, S.; Gong, Y.; Yang, S. Ultrafast Zn^{2+} Intercalation and Deintercalation in Vanadium Dioxide. *Adv. Mater.* **2018**, *30*, 1800762. [CrossRef]

20. Ke, L.; Dong, J.; Lin, B.; Yu, T.; Wang, H.; Zhang, S.; Deng, C. A NaV3(PO4)3@C hierarchical nanofiber in high alignment: Exploring a novel high-performance anode for aqueous rechargeable sodium batteries. *Nanoscale* **2017**, *9*, 12. [CrossRef]

21. Cui, F.; Wang, D.; Hu, F.; Yu, X.; Guan, C.; Song, G.; Xu, F.; Zhu, K. Deficiency and Surface Engineering Boosting Electronic and Ionic Kinetics in $NH_4V_4O_{10}$ for High-Performance Aqueous Zinc-Ion Battery. *Energy Storage Mater.* **2022**, *44*, 197–205. [CrossRef]

22. Xu, L.; Zhang, Y.; Zheng, J.; Jiang, H.; Hu, T.; Meng, C. Ammonium Ion Intercalated Hydrated Vanadium Pentoxide for Advanced Aqueous Rechargeable Zn-Ion Batteries. *Mater. Today Energy* **2020**, *18*, 100509. [CrossRef]

23. Jiang, Y.; Wu, Z.; Ye, F.; Pang, R.; Zhang, L.; Liu, Q.; Chang, X.; Sun, S.; Sun, Z.; Hu, L. Spontaneous Knitting Behavior of 6.7-nm Thin $(NH_4)_{0.38}V_2O_5$ Nano-Ribbons for Binder-Free Zinc-Ion Batteries. *Energy Storage Mater.* **2021**, *42*, 286–294. [CrossRef]

24. Tang, B.; Zhou, J.; Fang, G.; Liu, F.; Zhu, C.; Wang, C.; Pan, A.; Liang, S. Engineering the Interplanar Spacing of Ammonium Vanadates as a High-performance Aqueous Zinc-Ion Battery Cathode. *J. Mater. Chem. A* **2019**, *7*, 940–945. [CrossRef]

25. Jia, X.; Liu, C.; Neale, Z.G.; Yang, J.; Cao, G. Active Materials for Aqueous Zinc Ion Batteries: Synthesis, Crystal Structure, Morphology, and Electrochemistry. *Chem. Rev.* **2020**, *120*, 7795–7866. [CrossRef]

26. Wang, H.; Jing, R.; Shi, J.; Zhang, M.; Jin, S.; Xiong, Z.; Guo, L.; Wang, Q. Mo-doped $NH_4V_4O_{10}$ with Enhanced Electrochemical Performance in Aqueous Zn-Ion Batteries. *J. Alloys Compd.* **2021**, *858*, 158380. [CrossRef]

27. Wu, T.; Lin, W. Boosting Proton Storage in Layered Vanadium Oxides for Aqueous Zinc−Ion Batteries. *Electrochim. Acta* **2021**, *394*, 139134. [CrossRef]

28. Wu, T.; Li, Y.; Ni, K.; Li, T.; Lin, W. Vanadium Oxides Obtained by Chimie Douce Reactions: The Influences of Transition Metal Species on Crystal Structures and Electrochemical Behaviors in Zinc–Ion Batteries. *J. Colloid. Interf. Sci.* **2022**, *608*, 3122–3129. [CrossRef]

29. Zhu, T.; Mai, B.; Hu, P.; Liu, Z.; Cai, C.; Wang, X.; Zhou, L. Ammonium Ion and Structural Water Co-Assisted Zn^{2+} Intercalation/De-Intercalation in $NH_4V_4O_{10} \cdot 0.28H_2O$. *Chin. J. Chem.* **2021**, *39*, 1885–1890. [CrossRef]

30. Sun, R.; Qin, Z.; Liu, X.; Wang, C.; Lu, S.; Zhang, Y.; Fan, H. Intercalation Mechanism of the Ammonium Vanadate ($NH_4V_4O_{10}$) 3D Decussate Superstructure as the Cathode for High-Performance Aqueous Zinc-Ion Batteries. *ACS Sustainable Chem. Eng.* **2021**, *9*, 11769–11777. [CrossRef]

31. Zhang, W.; Tang, C.; Lan, B.; Chen, L.; Tang, W.; Zuo, C.; Dong, S.; An, Q.; Luo, P. $K_{0.23}V_2O_5$ as A Promising Cathode Material for Rechargeable Aqueous Zinc Ion Batteries with Excellent Performance. *J. Alloys Compd.* **2020**, *819*, 152971. [CrossRef]

32. Zhang, G.; Wu, T.; Zhou, H.; Jin, H.; Liu, K.; Luo, Y.; Jiang, H.; Huang, K.; Huang, L.; Zhou, J. Rich Alkali Ions Preintercalated Vanadium Oxides for Durable and Fast Zinc-Ion Storage. *ACS Energy Lett.* **2021**, *6*, 2111–2120. [CrossRef]

33. Feng, Z.; Zhang, Y.; Sun, J.; Liu, Y.; Jiang, H.; Cui, M.; Hu, T.; Meng, C. Dual Ions Enable Vanadium Oxide Hydration with Superior Zn^{2+} Storage for Aqueous Zinc-Ion Batteries. *Chem. Eng. J.* **2022**, *433*, 133795. [CrossRef]

34. Zong, Q.; Wang, Q.; Liu, C.; Tao, D.; Wang, J.; Zhang, J.; Du, H.; Chen, J.; Zhang, Q.; Cao, G. Potassium Ammonium Vanadate with Rich Oxygen Vacancies for Fast and Highly Stable Zn-Ion Storage. *ACS Nano* **2022**, *16*, 4588–4598. [CrossRef]

35. Chine, M.K.; Sediri, F.; Gharbi, N. Solvothermal Synthesis of V_4O_9 Flake-Like Morphology and its Photocatalytic Application in the Degradation of Methylene Blue. *Mater. Res. Bull.* **2012**, *47*, 3422–3426. [CrossRef]

36. Subba Reddy, C.V.; Jin, A.-P.; Han, X.; Zhu, Q.-Y.; Mai, L.-Q.; Chen, W. Preparation and Characterization of ($PVP + V_2O_5$) Cathode for Battery Applications. *Electrochem. Commun.* **2006**, *8*, 279–283. [CrossRef]

37. Zhang, J.; Wang, M.; Zeng, M.; Li, X.; Chen, L.; Yang, Z.; Chen, J.; Guo, B.; Ma, Z.; Li, X. Sulfite Modified and Ammonium Ion Intercalated Vanadium Hydrate with Enhanced Redox Kinetics for Aqueous Zinc Ion Batteries. *J. Power Sources* **2021**, *496*, 229832. [CrossRef]

38. Dai, X.; Wan, F.; Zhang, L.; Cao, H.; Niu, Z. Freestanding Graphene/VO_2 Composite Films for Highly Stable Aqueous Zn-ion Batteries with Superior Rate Performance. *Energy Storage Mater.* **2019**, *17*, 143–150. [CrossRef]

39. Yu, X.; Hu, F.; Cui, F.; Zhao, J.; Guan, C.; Zhu, K. The Displacement Reaction Mechanism of the CuV_2O_6 Nanowire Cathode for Rechargeable Aqueous Zinc Ion Batteries. *Dalton Trans.* **2020**, *49*, 1048–1055. [CrossRef]

40. Tang, B.; Fang, G.; Zhou, J.; Wang, L.; Lei, Y.; Wang, C.; Lin, T.; Tang, Y.; Liang, S. Potassium Vanadates with Stable Structure and Fast Ion Diffusion Channel as Cathode for Rechargeable Aqueous Zinc-Ion Batteries. *Nano Energy* **2018**, *51*, 579–587. [CrossRef]

41. He, T.; Ye, Y.; Li, H.; Weng, S.; Zhang, Q.; Li, M.; Liu, T.; Cheng, J.; Wang, X.; Lu, J.; et al. Oxygen-Deficient Ammonium Vanadate for Flexible Aqueous Zinc Batteries with High Energy Density and Rate Capability at −30 °C. *Mater. Today* **2021**, *43*, 53–61. [CrossRef]

42. Mannix, A.J.; Zhou, X.-F.; Kiraly, B.; Wood, J.D.; Alducin, D.; Myers, B.D.; Liu, X.; Fisher, B.L.; Santiago, U.; Guest, J.R.; et al. Synthesis of Borophenes: Anisotropic, Two Dimensional Boron Polymorphs. *Science* **2015**, *350*, 1513–1516. [CrossRef]

43. Chao, D.; Liang, P.; Chen, Z.; Bai, L.; Shen, H.; Liu, X.; Xia, X.; Zhao, Y.; Savilov, S.V.; Lin, J.; et al. Pseudocapacitive Na-Ion Storage Boosts High Rate and Areal Capacity of Self-Branched 2D Layered Metal Chalcogenide Nanoarrays. *ACS Nano* **2016**, *10*, 10211–10219. [CrossRef]

44. Augustyn, V.; Come, J.; Lowe, M.A.; Kim, J.W.; Taberna, P.L.; Tolbert, S.H.; Abruna, H.D.; Simon, P.; Dunn, B. High-rate Electrochemical Energy Storage through Li$^+$ Intercalation Pseudocapacitance. *Nat. Mater.* **2013**, *12*, 518–522. [CrossRef]
45. Weppner, W.; Huggins, R. Determination of the Kinetic Parameters of Mixed-Conducting Electrodes and Application to the System Li3Sb. *J. Electrochem. Soc.* **1977**, *124*, 1569–1578. [CrossRef]
46. Liu, X.; Xu, G.; Zhang, Q.; Huang, S.; Li, L.; Wei, X.; Cao, J.; Yang, L.; Chu, P.K. Ultrathin Hybrid Nanobelts of Single-Crystalline VO$_2$ and Poly(3,4-ethylenedioxythiophene) as Cathode Materials for Aqueous Zinc Ion Batteries with Large Capacity and High-Rate Capability, Layered Vanadium Oxides with Proton and Zinc Ion Insertion for Zinc Ion Batteries. *J. Power Sources* **2020**, *463*, 228223.
47. Liu, W.; Dong, L.; Jiang, B.; Huang, Y.; Wang, X.; Xu, C.; Kang, Z.; Mou, J.; Kang, F. Layered Vanadium Oxides with Proton and Zinc Ion Insertion for Zinc Ion Batteries. *Electrochim. Acta* **2019**, *320*, 134565. [CrossRef]
48. Wan, F.; Zhang, L.; Dai, X.; Wang, X.; Niu, Z.; Chen, J. Aqueous Rechargeable Zinc/Sodium Vanadate Batteries with Enhanced Performance from Simultaneous Insertion of Dual Carriers. *Nat. Commun.* **2018**, *9*, 1656. [CrossRef]
49. Ge, J.; Wang, B.; Wang, J.; Zhang, Q.; Lu, B. Nature of FeSe$_2$/N-C Anode for High Performance Potassium Ion Hybrid Capacitor. *Adv. Energy Mater.* **2020**, *10*, 1903277. [CrossRef]